J Mater Sci (2022) 57:3468–3485

Electronic materials

Third-order optical nonlinearities and high-order harmonics generation in Ni-doped $CsPbBr_3$ nanocrystals using single- and two-color chirped pulses

Srinivasa Rao Konda[1,*], Venugopal Rao Soma[2], Rashid A. Ganeev[1,3], Murali Banavoth[4], Ravi Ketavath[4], and Wei Li[1,*]

[1] *GPL, State Key Laboratory of Applied Optics, Changchun Institute of Optics, Fine Mechanics and Physics, Chinese Academy of Sciences, Changchun 130033, China*
[2] *Advanced Center of Research in High Energy Materials (ACRHEM), University of Hyderabad, Hyderabad, Telangana 500046, India*
[3] *Laboratory of Nonlinear Optics, University of Latvia, Riga LV-1586, Latvia*
[4] *Solar Cells and Photonics Research Laboratory, School of Chemistry, University of Hyderabad, Hyderabad, Telangana 500046, India*

Received: 18 October 2021
Accepted: 31 December 2021
Published online: 20 January 2022

ABSTRACT

Organic–inorganic lead halide perovskite nanocrystals (NCs) have received the phenomenal attention of researchers in the last few years due to their advanced optical properties and developments in simple synthetic procedures. In this work, we demonstrate the effect of Ni-dopant on the ultrafast third-order nonlinear optical (NLO) properties of two-dimensional (2D) $CsPbBr_3$ NCs using 60 fs laser pulses at a wavelength of 400 nm. Based on the probe pulse intensity, pure $CsPbBr_3$ NCs exhibited saturable absorption and reverse saturable absorption (RSA). The doping of NCs by Ni at different concentrations significantly modified the nonlinear absorption mechanism where the RSA was followed by the SA with growing input laser intensity. The nonlinear refractive index of Ni-doped $CsPbBr_3$ NCs decreased when compared with the pure $CsPbBr_3$. In addition, the NLO properties of these 2D NCs are correlated with the efficiency of the high-order harmonics generated during propagation of the two-color (800 + 400 nm) and single-color (800 nm) chirp-free (35 fs) and negatively/positively chirped pulses through the laser-induced plasmas produced on the surface of undoped and Ni-doped perovskite NCs. The ablation of Ni-doped NCs allowed increasing the harmonic yield compared to undoped $CsPbBr_3$ NCs. Our studies undoubtedly demonstrate the advanced lower and higher order NLO properties of Ni-doped 2D $CsPbBr_3$ NCs.

Handling Editor: Pedro Camargo.

Address correspondence to E-mail: ksrao@ciomp.ac.cn; weili1@ciomp.ac.cn

https://doi.org/10.1007/s10853-022-06871-z

GRAPHICAL ABSTRACT

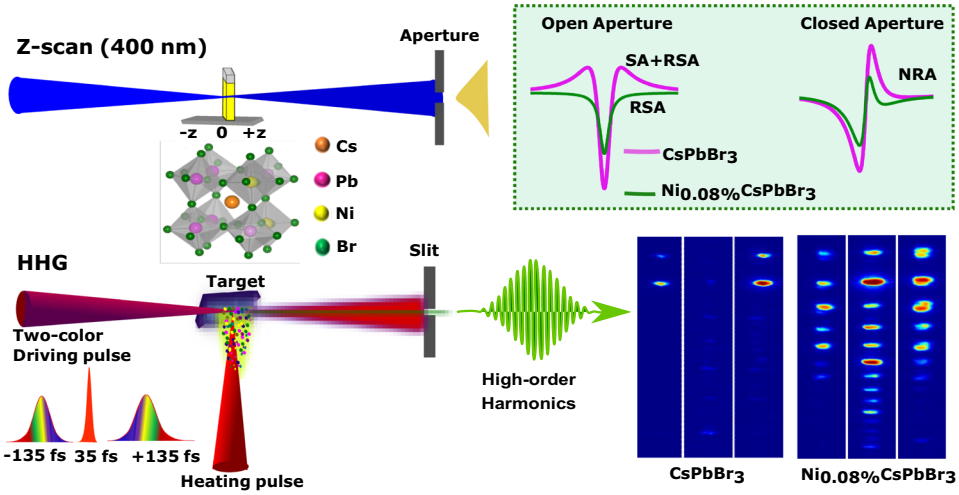

Introduction

Lead halide-based perovskite nanocrystals (NCs) have unique and venerable photophysical properties, which permitted their efficient application in various optoelectronic devices such as photodetectors, light-emitting diodes, solar cells, and lasers. Their optical, optoelectronic, photonic, and third-order nonlinear optical (NLO) properties were frequently reported and reviewed [1–16]. The excited-state dynamics (pumped with 400 nm), NLO, and photoluminescent properties of the undoped and Ni-doped $CsPbBr_3$ NCs were explored in our recent work [17]. It was demonstrated that the photoluminescence (PL) yields from Ni-doped $CsPbBr_3$ NCs were higher than from pure $CsPbBr_3$ NCs. Further, the central wavelength was observed to vary in the PL spectra depending on the weight percentage of the dopant. In addition, a few research groups have explored the outstanding NLO properties of different perovskite nanomaterials such as (i) saturable absorption (SA) (ii) reverse saturable absorption (RSA) (iii) two-photon absorption (2PA) (iv) multiphoton absorption and (v) nonlinear refraction using different excitation wavelengths and input pulse durations [18–33]. However, there are very few reports of the NLO properties of these exotic molecules in the UV spectral region. Additionally, the high-order harmonics generation (HHG) in solids, gases, and laser-induced plasmas (LIPs) attracted great attention due to the necessary information of the efficient sources of coherent extreme ultraviolet (XUV) radiation [34–57]. Various capable solid materials and gas jets with control of driving pulse duration to obtain better conversion efficiencies and cut-off of harmonics were analyzed [40, 58–64]. Recently, Hussain et al. [65] have demonstrated HHG with spectral shifts in the obtained harmonics in silicon (Si) and zinc oxide (ZnO) achieved by scanning the focal position of the 85 fs driving pulses at a wavelength of 2.123 μm. The variations of the spectral shape and harmonic distribution from silver plasma using chirped pulses from the 793 nm, 44 fs laser pulses were also reported [66]. Those studies underlined the role of chirped pulses in enhancing the harmonic's emission. Surprisingly, there are hardly any reports on the understanding of the correlation between different NLO properties of these NCs, for instance, the HHG yield and the real and imaginary parts of nonlinear susceptibilities.

In this study, we report the NLO properties of undoped and Ni-doped $CsPbBr_3$ NCs using femtosecond pulses at the wavelength (λ) of 400 nm. We also analyze the high-order harmonics spectra using the positively and negatively chirped femtosecond laser pulses propagating through the plasmas

generated on the NCs surfaces. A correlation between the low-order NLO properties and the HHG in these NCs is discussed. The examination of innovative and effective materials (ablated Ni-doped NCs in the current case) in this way will allow achieving XUV radiation for a diversity of applications in attosecond physics and nonlinear spectroscopy [67–70].

Experimental details

Synthesis and characterization of nanocrystals

1 mM of $PbBr_2$ and 0.08 mM $NiBr_2$ were loaded into a three-neck round bottom flask containing 5 ml of 1-octadecene with 0.5 ml of dried oleic acid and dried olylamine (here, oleic acid and olylamine act as capping ligands). This was degassed for about one hour under vacuum (10^{-2} mbar) at 120 °C. The flask was subsequently flushed with nitrogen and heated to 150 °C. Later the temperature was raised to 210 °C and was kept for 5–10 minutes to reach the temperature. Subsequently, the cesium oleate solution was heated to the chosen reaction temperature (typically 150 °C) before 5 ml of 1 mM of cesium oleate (1 mM of $CsCO_3$, 20 ml of 1-octadecene, and 1.25 ml of oleic acid) solution was swiftly injected into the prepared precursor solution. After five seconds, the reaction mixer was cooled under an ice bath. Subsequently, we obtained the precipitated NCs by adding them with 5 ml of acetone.

The synthesis of Ni-doped $CsPbBr_3$ was confirmed by observing the change in NCs formation as both the Ni:Pb ratio vary during the synthesis [71]. Post-synthesis cation exchange procedures can incorporate divalent guest cations into $CsPbBr_3$ NCs, according to our findings. The aliovalent exchange of Cs^+ by smaller Ni^{+2} cations can substantially destabilize the perovskite structure significantly, necessitate charge compensation. As a result, we assumed that the solely isovalent exchange of Pb^{+2} by Ni^{+2} occurred. Chemical mapping was used to validate the incorporation and distribution of the guest cation using energy-dispersive X-ray spectroscopy (EDS) data [72]. Schematic illustration of the structural properties of $CsPbBr_3$ NCs before and after substitution of Pb^{+2} with 0.08 mM of Ni^{+2} ion is shown in Fig. 1.

Our previous works [17, 73] discussed the UV–Visible absorption spectra, PL characteristics, and surface morphologies of pristine ($CsPbBr_3$) NCs, 0.03 percent Ni, 0.05 percent Ni, 0.08 percent Ni, 0.1 percent Ni-doped $CsPbBr_3$ NCs using transmission electron microscopy (TEM) pictures. In a nutshell, the absorption spectra of $CsPbBr_3$ and $NiCsPbBr_3$ were measured in the 200–800 nm region using a UV–Visible-NIR spectrophotometer (Model UV 3600, M/s Shimadzu). The samples were organized by diluting 20 μL of the crude NCs solution in ~1 mL of toluene and placed in quartz cuvettes (1 cm). $CsPbBr_3$ and $NiCsPbBr_3$ had absorption peaks near 482 and 508 nm. The emission spectra were recorded using a spectrofluorometer (from Horiba Jobin Yvon) and the corresponding PL emission peaks were observed at 530 and 566 nm. Ni-doping did not introduce a new absorption band in $CsPbBr_3$ and the resultant excitation absorption of the $NiCsPbBr_3$ NCs shifts to the red spectral region. The lifetime of photogenerated charge carriers was determined by time-resolved photoluminescence. $NiCsPbBr_3$ had a longer lifetime (13.41 ns) compared to its pristine counterpart (11.38 ns), which can be considered as an advantage for application in LED devices [17]. The synthesized NCs had a square-like shape with an average size of ~20 nm, according to the TEM studies. These NCs possessed a well-defined crystalline structure; it was observed in the orthorhombic phase. The size and uniformity of attained NCs were influenced by the doping of Ni. The measured lattice fringe spacing for pure and 0.08 percent Ni was 0.394 nm and 0.390 nm, respectively, indicating that Ni-doped $CsPbBr_3$ NCs had a restricted size distribution.

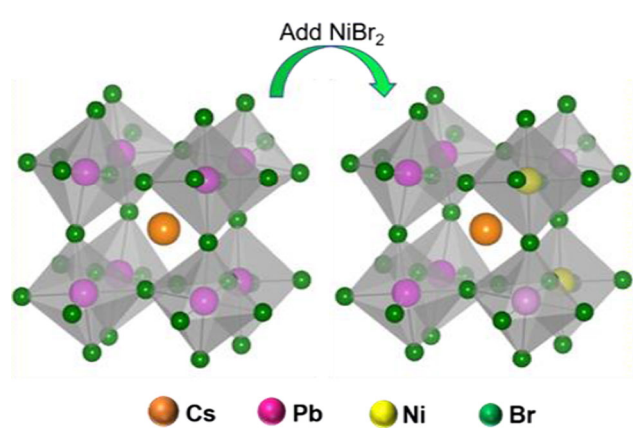

Figure 1 Schematic illustration of the structural properties of $CsPbBr_3$ NCs before and after substitution of Pb^{+2} with 0.08 mM of Ni^{+2} ion.

Z-scan measurements

The Ti: sapphire (Spectra-Physics, Model Spitfire Ace) laser system used in the present studies delivered linearly polarized 800 nm, 35 fs, 1 kHz pulses. The laser pulses were broadened to 60 fs before the focusing lens (200 mm focal length, beam waist radius w_o =16 μm) along the Z-scan path. The second harmonic (400 nm) of 800 nm radiation was generated using a 0.2 mm thick barium borate (BBO, type I) crystal and the 800 nm pulses were filtered using the color filter [Fig. 2(a)]. The pulse energies of 0.1 μJ (peak intensity (I_o) =2.6 $\times 10^{11}$ W/cm^2) and 0.15 μJ (I_o=3.9 $\times 10^{11}$ W/cm^2) were used to analyze the third-order NLO properties of the studied samples. The 1-mm thick fused silica cell filled with NCs suspension possessing a concentration of typically 4×10^{-4} mM was moved along the Z-axis of the focused laser beam as shown in Fig. 2a. For open-aperture (OA) and closed-aperture (CA) Z-scan measurements, after propagation of the sample, the two beams were collected by photodiodes 1 and 2, respectively. In the case of CA, the aperture was adjusted to allow the propagation of ~15% of the input beam. At each point, the photodiode signal versus position of the sample was monitored by a personal computer using a data acquisition program developed using LabVIEW.

HHG experimental layout

Figure 2b illustrates the schematic of the experimental setup used for HHG measurements. We used a Ti: Sapphire laser (800 nm, 35 fs) operated at 100 Hz pulse repetition rate. The 200 ps, 800 nm heating pulses (HP) from the same laser ablated the 2D NCs targets to create the plasma plumes. The harmonics spectra were obtained using the chirp-free single-color pump (SCP, 800 nm wavelength) and two-color pump (TCP, 800 nm + 400 nm wavelengths) of the LIPs produced on the surfaces of the studied samples. We also used the negatively and positively chirped 135 fs radiation from this laser as the driving pulses (DP) and compared the harmonic spectra generated using the above pulses with those produced by the chirp-free 35 fs pulses. The intensities of the chirp-free and chirped pulses in the focal plane were 4×10^{14} and 0.9×10^{14} W/cm^2, respectively. The chirp of the DPs was varied by changing the separation of the gratings in the pulse compressor of Ti: sapphire laser [66]. The chirp-free, negatively, and positively chirped pulses contain similar spectral components while showing a difference in their temporal characteristics and distribution of the spectral components along the laser pulse (see also Sect. 3.2). The details and description of the 2D NCs samples preparation for HHG measurements are presented in our earlier work [73]. Briefly, the NCs were dispersed in toluene solvents and then precisely drop-casted on the glass substrate until drying. The approximated length × width × thickness of NCs target was ~ 8 mm × 6 mm ×1 mm. The substrates with NCs were placed in the target chamber (Fig. 2b) and ablated by HPs. The DPs propagated through the plasma plumes approximately 0.2 mm above the target surface. The emitted harmonics from LIPs were directed to the XUV chamber, which consists of a gold-coated cylindrical mirror (CM), flat field grating (FFG), and microchannel plate (MCP). Finally, the harmonic spectra were recorded using a charge-coupled device camera (CCD).

Results and discussion

Third-order NLO properties of nanocrystals

The third-order NLO properties of five ($CsPbBr_3$ and Ni (0.03, 0.05, 0.08, and 0.1 %)-doped $CsPbBr_3$ NCs) samples are measured using the standard Z-scan technique at wavelength (λ) of 400 nm. From the OA and CA Z-scan measurements, one can obtain the nonlinear absorption coefficient (β), saturation intensity (I_{sat}), and nonlinear refractive index (γ) of these species. The normalized transmittance of studied samples in the case of RSA and combination of SA and RSA can be fitted by the following equations [74]

$$T_{\mathrm{RSA}}(z) \approx 1 - \frac{q}{2\sqrt{2}} \tag{1}$$

$$T_{\mathrm{SA+RSA}}(z) \approx \left(1 - \frac{q}{2\sqrt{2}}\right) \times \frac{I_o}{I_{sat}(x^2+1)} \tag{2}$$

Here $q = \beta I_o L_{\mathrm{eff}}/(1+z^2/z_o^2)$, $x= z/z_o$, $z_o= k\ (w_o)^2/2$ is the Rayleigh length. w_o is the beam waist radius, $k = 2\pi/\lambda$ is the wavenumber, I_o is the intensity of the laser beam in the focal plane. L_{eff} = [1-exp (-α_o L)]/α_o is defined as the effective length of the samples, α_o is the linear absorption coefficient of sample, and L is the thickness of the sample.

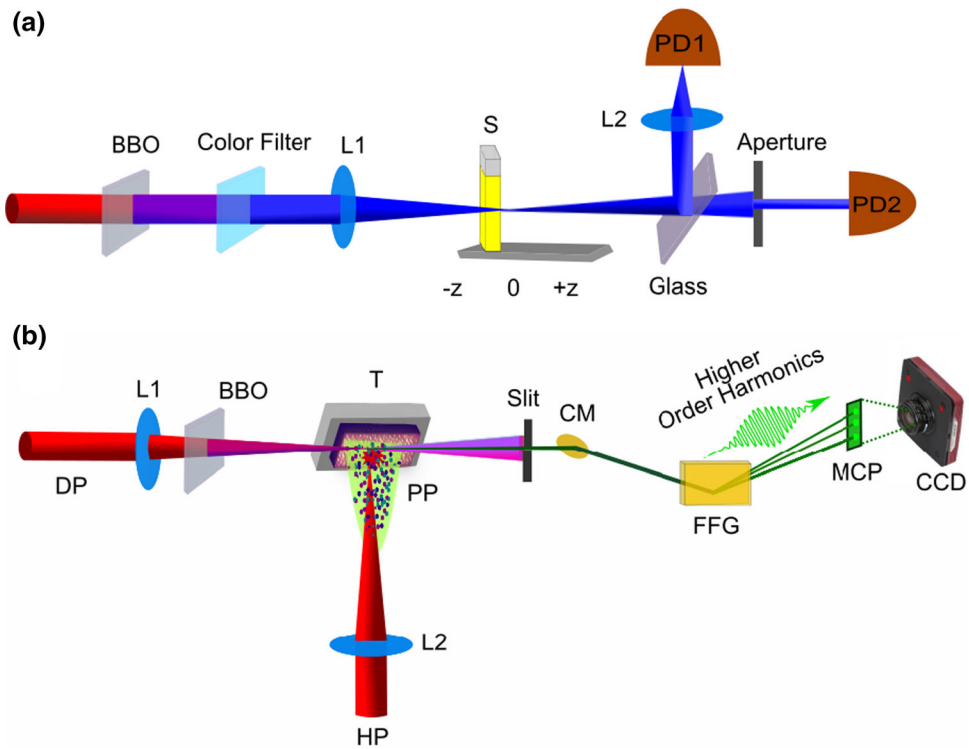

Figure 2 Experimental layouts for Z-scan and HHG measurements. **a** Z-scan scheme. BBO: barium borate crystal; L1: focusing lens (f=200 mm), S: sample (1-mm thick cell filled with NCs suspension); L2: focusing lens for the collection of the propagated beam (f = 200 mm); PD1 and PD2: photodiodes for the measurements of propagated radiation in the case of open-aperture and closed-aperture schemes, respectively. **b** HHG scheme. DP: 800 nm driving pulses; L1: focusing lens (f = 500 mm) for the driving pulses; BBO: barium borate crystal; T: target; PP: plasma plume; L2: focusing lens (f = 200 mm for the heating pulses; HP: 200 ps, 800 nm heating pulses; CM: gold-coated cylindrical mirror; FFG: flat field grating; MCP: microchannel plate; CCD: charge-coupled device camera.

The normalized transmittance in the presence of nonlinear refraction and absorption (NRA) can be written as [75]

$$T_{\mathrm{NRA}}(z) = 1 + \frac{2(-\rho x^2 + 2x - 3\rho)}{(x^2+9)(x^2+1)}\Delta\Phi_o \quad (3)$$

Here $\Delta\Phi_o = k\gamma I_o L_{\mathrm{eff}}$ and $\rho = \beta/2k\gamma$. Correspondingly, the nonlinear refraction index can be determined as

$$\gamma = \frac{\lambda\Delta\Phi_o}{2\pi I_o L_{eff}} \quad (4)$$

Figures 3 and 4 show the OA and CA Z-scan curves for $CsPbBr_3$ and Ni (0.03, 0.05, 0.08 and 0.1 %)-doped $CsPbBr_3$ NCs at input laser intensities I_o = 2.6 × 10^{11} W/cm^2, and 3.9 × 10^{11} W/cm^2, respectively. Five measurements were carried out for each OA and CA Z-scans and the average data are presented in the corresponding Figs. 3 and 4.

For $CsPbBr_3$ NCs, the OA Z-scan curves illustrated an upward trend at the outer part of the focal plane, suggesting the presence of SA. However, once the sample approached the focus, the Z-scan data depicted a sharp dip in the transmittance representing the appearance of RSA. It was also observed that the RSA increased with the growth of input intensities (Fig. 3, $CsPbBr_3$ panels). The corresponding I_{sat} for pure $CsPbBr_3$ NCs at I_o = 2.6 × 10^{11} W/cm^2 was estimated to be 2×10^{11} W/cm^2. Whereas in the case of Ni-doped $CsPbBr_3$ NCs, the Z-scan curves demonstrated RSA and the dip moved in the upward direction compared to pristine $CsPbBr_3$ as shown in Fig. 3a, b. We observed that Ni-dopant presence demonstrated a massive impact on the nonlinear absorption process. At the outer part of the focal plane, Ni-counterparts possessed RSA and at the focus they depicted SA, which was confirmed by dividing the pure $CsPbBr_3$ contribution from the Z-scans of Ni-doped $CsPbBr_3$ NCs. The corresponding divided Z-scan data are shown in Fig. 5a, b. The plots also show that the increment in the percentile

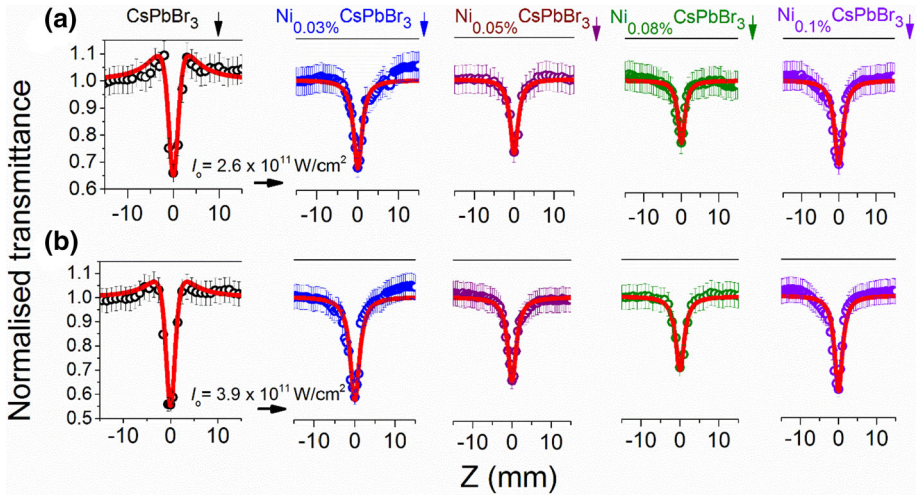

Figure 3 Open-aperture Z-scan curves in the case of pristine and Ni-doped $CsPbBr_3$ nanocrystals, at the **a** 2.6×10^{11} and **b** 3.9×10^{11} W/cm^2 intensities of laser pulses. Open symbols represent experimental data points while the solid lines are theoretical fits.

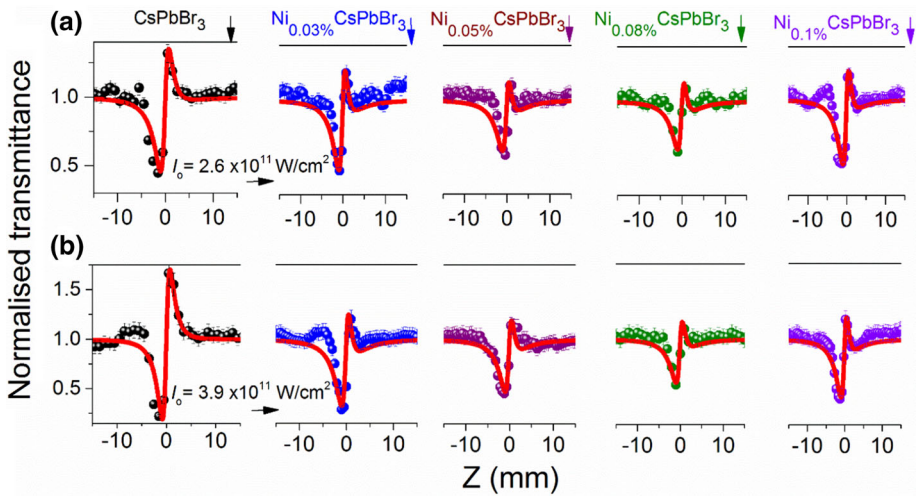

Figure 4 Closed-aperture Z-scan curves in the case of pristine and Ni-doped $CsPbBr_3$ nanocrystals at the **a** 2.6×10^{11} and **b** 3.9×10^{11} W/cm^2 intensities of laser pulses. Solid symbols represent experimental data points while the solid lines are theoretical fits.

change of Ni-dopants depicts a nonlinear growth of the saturable absorption peaks at focus. The conclusion about the growing role of RSA was also confirmed during the division of the pure $CsPbBr_3$ contribution from Ni-doped $CsPbBr_3$ NCs in the case of CA measurements (see data presented in Fig. 5(c, d)).

Pure and doped NCs illustrated a self-focusing behavior, evident from the CA Z-scan data presented in Fig. 4. However, the addition of Ni led to a decrease in self-focusing. Consequently, Ni dopants showed the self-defocusing properties and the nonlinear refractive index of dopants has a negative sign (see Figs. 5c, d, 6b]. The experimental data of OA and CA measurements at $I_o = 2.6 \times 10^{11}$ W/cm^2 and 3.9×10^{11} W/cm^2 of the undoped and doped NCs are fitted using Eqs. 1, 2 and 3, respectively and the calculated NLO parameters are listed in Table 1. Whereas, for ratio of $NiCsPbBr_3$ NCs to the pure $CsPbBr_3$ NCs the obtained I_{sat} and γ values are shown in Table 2.

In this work, we have pumped with 400 nm (3.0 eV) pulses for extracting the NLO coefficients of pure $CsPbBr_3$ and $NiCsPbBr_3$ NCs. The obtained results demonstrate that the $NiCsPbBr_3$ NCs possessed RSA and self-focusing properties. However, these processes magnitude were found to be decreased with the growth of the Ni concentration. Consequently, it was observed that for $NiCsPbBr_3$ NCs possess lower β and γ values compared to pure $CsPbBr_3$ NCs. This is due to the fact that the Ni dopants possess negative nonlinear absorption coefficient (due to the influence of SA) and negative nonlinear refractive index compared to the pure $CsPbBr_3$ NCs. Correspondingly, the studied mixture (Ni + $CsPbBr_3$ NCs) shows smaller values of β and γ compared to the pure $CsPbBr_3$ NCs. The mechanisms of Ni dopants are extracted from

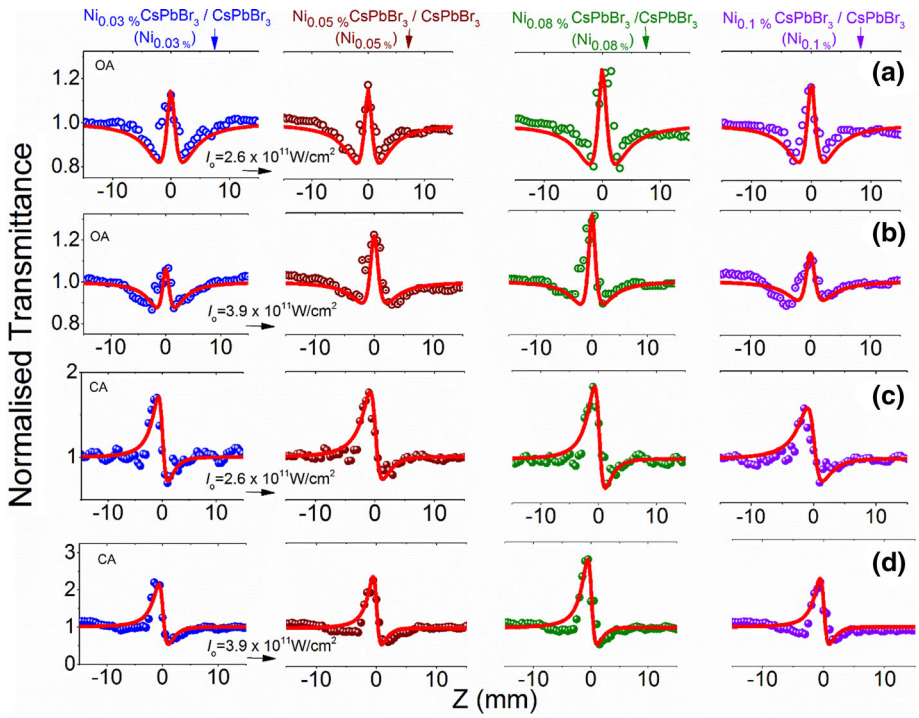

Figure 5 The ratio of Z-scans at 2.6×10^{11} and 3.9×10^{11} W/cm^2 for the Ni-doped $CsPbBr_3$ NCs with regard to the pure $CsPbBr_3$ in the case of **a**, **b** OA and **c**, **d** CA measurements. Open and solid symbols represent experimental data points while the solid lines are theoretical fits..

both OA and CA measurements by dividing the pure $CsPbBr_3$ NCs data to $NiCsPbBr_3$ data. Meanwhile, after the deduction of pure $CsPbBr_3$ contribution from $NiCsPbBr_3$ NCs, though Ni doped samples demonstrated decreased I_{sat} values with respect to their % changes. In this case, the materials transmitted higher power than the pure NCs. These materials can be used for optical limiting and/or optical switching applications. Furthermore, we believe these materials have the potential for optical communications/sensing applications since the nonlinearities can be tuned by changing the dopant and the doping levels. See, for example, a recent report by Gopala Krishna et al. [76] wherein they demonstrated that doping resulted in the passivation of surface defect states, which improved the photoluminescence

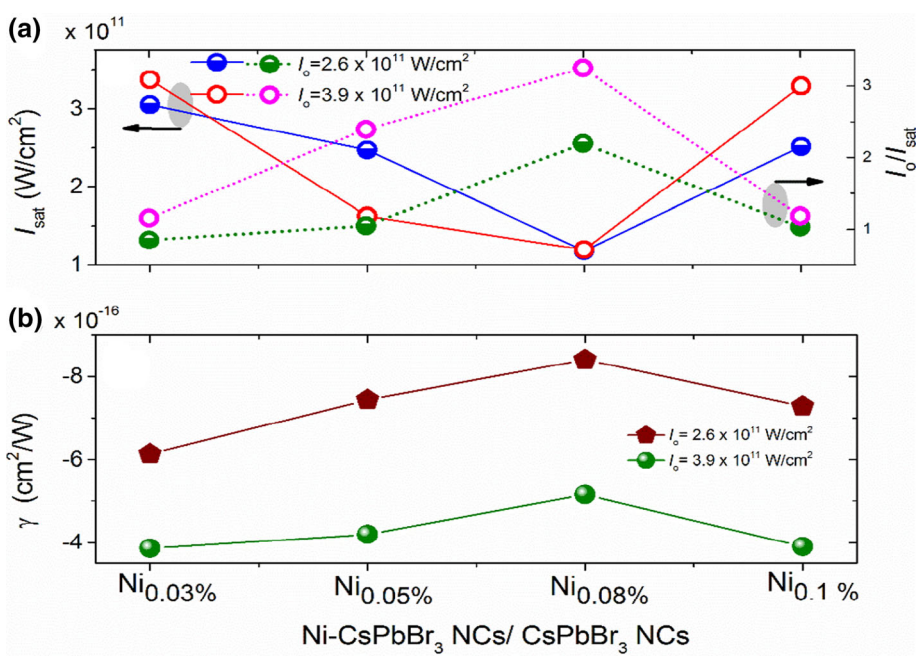

Figure 6 The variations of saturation intensities (left: Y-axis) and ratios of I_o/I_{sat} (right: Y-axis) (**a**) and nonlinear refraction indices (**b**) at different concentrations of Ni using two intensities (I_o= 2.6×10^{11} W/cm^2 and 3.9×10^{11} W/cm^2).

Table 1 Summary of the NLO parameters of studied samples at λ = 400 nm

Samples	At I_o=2.6 × 10^{11} W/cm^2		At I_o=3.9 × 10^{11} W/cm^2	
	$\beta(\times10^{-11})$ cm/W	$\gamma(\times10^{-16})$ cm^2/W	$\beta(\times10^{-11})$ cm/W	$\gamma(\times10^{-16})$ cm^2/W
$CsPbBr_3$	4.88±0.23	6.6±0.33	6.52±0.32	7.58±0.37
$Ni_{0.03\%}$-$CsPbBr_3$	4.37±0.21	5.09±0.25	3.83±0.19	4.20±0.21
$Ni_{0.05\%}$ -$CsPbBr_3$	3.59±0.17	3.40±0.17	3.06±0.15	3.27±0.16
$Ni_{0.08\%}$ -$CsPbBr_3$	3.03±0.15	3.30±0.16	2.70±0.13	2.79±0.13
$Ni_{0.10\%}$ -$CsPbBr_3$	4.06±0.20	4.78±0.23	3.56±0.17	3.60±0.18

Table 2 Summary of the NLO parameters for only Ni NCs. The NLO parameters were obtained from division data of Ni $CsPbBr_3$ to pure $CsPbBr_3$ NCs

Samples (%Ni$CsPbBr_3$/ $CsPbBr_3$)	At I_o=2.6 × 10^{11} W/cm^2		At I_o=3.9 × 10^{11} W/cm^2	
	$I_{sat}(\times10^{11})$ W/cm^2	-$\gamma(\times10^{-16})$ cm^2/W	$I_{sat}(\times10^{11})$ W/cm^2	-$\gamma(\times10^{-16})$ cm^2/W
$Ni_{0.03\%}$	3.05	6.13	3.37	3.86
$Ni_{0.05\%}$	2.46	7.43	1.62	4.19
$Ni_{0.08\%}$	1.18	8.40	1.19	5.16
$Ni_{0.10\%}$	2.51	7.29	3.29	3.90

quantum yield and PL lifetime of the $CsPbBr_3$ nanocrystals. Figure 6 shows the variations of saturation intensities and nonlinear refractive indices of Ni components at the input intensities I_o= 2.6 ×10^{11} and 3.9×10^{11} W/cm^2, respectively. The 0.05 and 0.08% Ni-containing NCs possessed lower saturation intensities than the 0.03 and 0.1% Ni.

We also deduced that with further growth of laser intensity, the NLO coefficients decreased. The nonlinear coefficients ideally should not depend on excitation fluence. It is true for the small intensities of the probe pulses. It is well known in the literature that increasing input intensity will result in further excitation from the higher energy levels (conduction band in this case). Depending on the input peak intensities, a SA process can switch to RSA process and vice-versa [see, for example, Ref. [82] in the case of gold nanoparticles prepared by laser ablation techniques and Ref. [83] in the case of Au coated triangular Ag-Au nanostructures]. When there are excitations into the higher energy states, the NLO coefficients get modified with the presence of other/higher-order NLO processes.

We observed the tendency of NLO coefficients to look similar at two used intensities of laser pulses, i.e., at 2.6 ×10^{11} W/cm^2 and 3.9×10^{11} W/cm^2. It is assumed that, at higher input laser intensities, the valence band electrons are trapped in the higher levels of the conduction band. Probably this led to a slight decrease in the NLO coefficients. Moreover, multiple factors contribute to the NLO response of the materials. In brief, the influence of the pumping wavelength, input pulse duration, and the sizes/shapes of nanoparticles/quantum dots/nanocrystals significantly affect the NLO parameters. Zhu et al. reported β and γ values of $CsPbBr_3$ QDs using excitation wavelengths of 700–1200 nm at 30 kHz repetition, 34–172 fs pulses, and they reported that β and γ were considerably different with respect to different excitation wavelengths [84]. Analysis of size-dependent off-resonant nonlinear optical properties of gold nanoparticles showed the variation of the sign of nonlinear refraction index and nonlinear absorption coefficient for different Au NPs [85]. The same can be said about the influence of pulse duration of the probe radiation on the nonlinear optical response of nanoparticles [86]. We have systematically compared the NLO parameters at different excitation parameters for different sizes and shapes as of $CsPbBr_3$ perovskites reported by other research groups, as shown in Table 3.

The typical energy level diagrams of $CsPbBr_3$, as well as Ni-doped $CsPbBr_3$ NCs, are illustrated in Fig. 7. We believe that the transitions responsible for RSA are different for Ni-doped $CsPbBr_3$ NCs compared to pristine $CsPbBr_3$ NCs because of the

modification of their energy level structure due to doping. It is known that Ni doping reduces the bandgap and induces the defect states in the bandgap region (closer to the conduction band). Possibly, with a higher doping percentage, the density of defect states also increases. Furthermore, at λ = 400 nm, the absorbance in doped NCs is higher than that in pure NCs. Once the electrons are excited to the conduction band (with 400 nm pump photon corresponding to ~3.0 eV energy), the saturation effect dominates at lower peak intensities since the NCs possess strong linear absorption. However, with increasing peak intensities, there is a possibility of RSA (as shown in Fig. 7).

In pure NCs, the RSA is dominant even at lower peak intensities. The pertinent issue here is the depopulation from excited states to either the lower part of the conduction band (pure case) or to either lower part of the conduction band followed by a transition to the defect states (in doped case), which will possibly affect further absorption leading to either stronger RSA or slightly weaker RSA, depending on the possible scenarios, and thereby influencing the I_{sat}. The lifetimes (intra-band relaxation) of the electron, typically in the femtosecond time domain, in the excited states are significant for further absorption through RSA. Further detailed high-resolution pump-probe investigations are necessary to explore this effect.

We estimated the bandgap of $CsPbBr_3$ as 2.34 eV (Fig. 7a), which is close to the one reported in Ref. [87]. The doped divalent element can form the defect levels in the perovskite structure, which trap the electrons and reduce the recombination of charge carriers [71]. Ni^{2+} has partially filled d-orbital and thus can create the donor levels in the bandgap of $CsPbBr_3$, leading to a decrease in bandgap (Fig. 7b). The nonlinear absorption mechanism depends on the material's bandgap and pumping photon energy. The initial absorption process for an electron moving from valence to conduction band can be quantified by considering the ratio between material bandgap and pump photon energy. It is estimated that the ratio values equal to one 1 or less shows saturable absorption, i.e., the case when the pump photon energy is equal or higher than the bandgap of material leads to SA. However, the total nonlinear absorption process depends on the intensity of photon energy and energy levels of the conduction band. In the current case, pure $CsPbBr_3$ NCs demonstrated SA at lower intensities (out of focal plane). When intensity of pulses reached peak values, the RSA is predominated (for Z-scan results, please see Fig. 3). Similarly, if the photon energy is lower than the bandgap of a material then it leads to a multi-photon absorption process. Depending on pump photon energy, the initial absorption process may lead to 2PA, 3PA, 4PA, and 5PA, etc. For example, the ratio values for 2.34 eV to pump photon energy between 700–1200 nm range; the absorption process agrees with previous work reported by Chenyang Zhu et al. [84], i.e., at 700–1100 nm the $CsPbBr_3$ QDs possess 2PA and at 1100–1200 nm having 3PA.

In the case of $NiCsPbBr_3$, the addition of Ni probably led to a decrease in the bandgap (Fig. 7b). Therefore, at the peak intensities of pump wavelength, Ni NCs possessed SA and the saturation varies depending on the concentration of Ni NCs. It was observed that the absorption process for pure NCs is SA+RSA. In the case of Ni NCs, near to the focus, they possess SA; due to this effect near the focus, there is a decrease in the RSA compared to pure NCs (see Fig. 3). In conclusion, the NLO process could be influenced by pumping wavelength and pulse duration and the size and shape of the small-sized species. Therefore, it is necessary to explore the NLO properties of materials at required pump wavelengths along with different pulse durations.

In the case of magnetic properties of the synthesized materials, the electron and hole are subjected to various Zeeman interactions in the presence of a magnetic field. As a result, the combined electron-hole energy level broadens and changes, affecting the PL line width appropriately [88]. The presence of a magnetic field results in a net increase in triplet excitons due to the formation of anti-parallel (singlet state) and parallel (triplet state) spin states excitons. When charge-separated states are achieved, then more electrons and holes with parallel spin states will be formed [89]. An elaborative study about the magnetic properties of the synthesized material has to be explored further.

HHG from LIPs containing nanocrystals using chirp-free 35 fs and chirped 135 fs pulses

The low-order NLO properties of Ni-doped $CsPbBr_3$ NCs at 400 nm wavelength can be used in different applications such as light-emitting diodes,

Table 3 Summary of the ultrafast NLO properties/coefficients of various perovskite materials

Samples	Size distribution	Excitation details	NLO process	β (cm/GW)	I_{sat} (GW/cm^2)	γ (cm^2/W)	Ref.
$CsPbBr_3$ materials							
Square NCs	~ 20 nm	800 nm, 70fs, 1 kHz	2PA	3.9×10^{-2}		3.52×10^{-12}	[17]
Cubic NCs	~ 9 nm	800 nm, 70 fs, 1 kHz	2PA	0.097			[25]
Nano cubes:	~12.4 nm	800 nm, 50 fs, 1 kHz	2PA	0.091			[21]
QDs: spherical(blue emissive)	5 nm	800 nm, 130 fs, 76 MHz	2PA	– 1.71		-5.18×10^{-15}	
QDs: nano cubes (green emissive)	~17 nm	800 nm, 130 fs, 76 MHz	2PA	– 0.68	0.011	1.99×10^{-15}	[32]
Nanosheet:	104.6 nm	800 nm; 80 fs	2PA	10.94	3.12		
	195.4 nm	800 nm; 80 fs	2PA	4.73	4.79		[77]
Mono-crystal	1000 nm	30 ps, 50 Hz	2PA	5.00			[29]
Nanocrystal film:		1060 nm,500 ps	SA		10.7		[78]
Nano cubes:	10-16 nm	1064 nm, 1 ns, 20 kHz	3PA	0.9–1.1 cm^3/GW^2	0.8-1	$0.8\text{-}1.2\times10^{-12}$	[79]
Single crystal:		1200 nm	3PA	γ = 0.14 cm^3/GW^2			[79]
		2050-2300 nm, 50 fs.	5PA	$\eta\delta_5 = (0.09-6.5) \times 10^{-136}$ cm^{10} s^4 photon^{-4}			[18]
Other perovskites							
QDs cubes:	~12.4 nm	800 nm, 50fs, 1 kHz	2PA	0.054			
$CsPbCl_2Br$:				0.064			[21]
$Cs_2AgIn_{0.9}Bi_{0.1}Cl$ NCs	1-5nm	800 nm, 57fs	2PA	6.88		55×10^{-13}	[80]
$CsPbI_{1.5}Br_{1.5}$	~40 µm	1064 nm, 2 ps,58 MHz	2PA	0.94			[81]

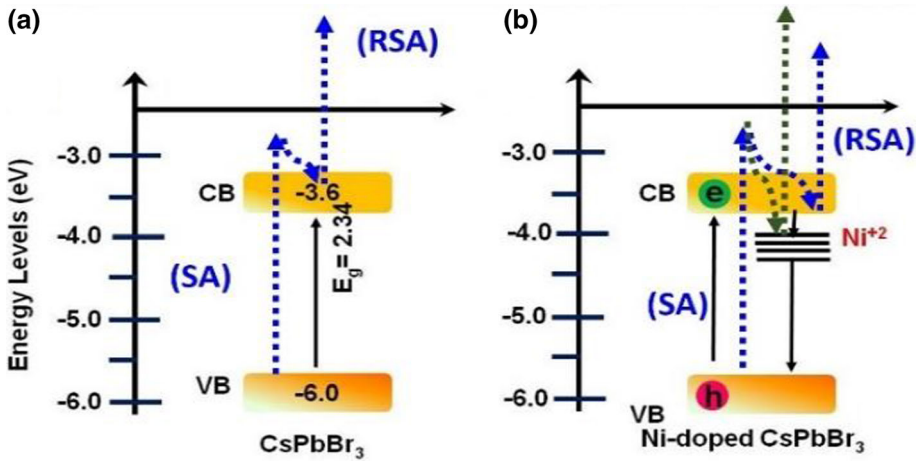

Figure 7 Energy levels of **a** $CsPbBr_3$ and **b** Ni-doped $CsPbBr_3$ nanocrystals. Also depicted are the transitions for RSA and SA (blue dotted lines).

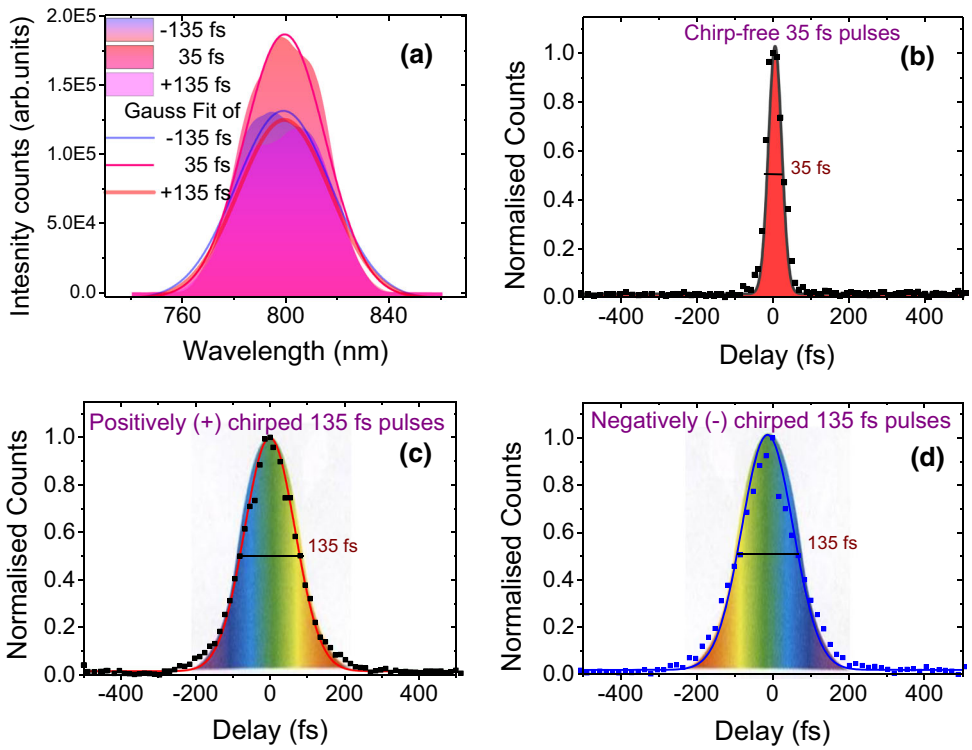

Figure 8 Spectral shapes and spectro-temporal distributions of used laser pulses for HHG. **a** Spectra of chirp-free 35 fs pulses, negatively chirped 135 fs pulses, and positively chirped 135 fs pulses. **b** Autocorrelation trace of 35 fs pulses. Spectral distribution along these chirp-free pulses represents the homogeneously distributed red and blue components in both the leading and trailing parts of the laser pulse. **c** Autocorrelation trace and spectral distribution along the positively chirped 135 fs pulses. The red component is moved toward the leading front of the pulse. **d** Autocorrelation trace and spectral distribution along the negatively chirped 135-fs pulses. The blue component is moved toward the leading front of the pulse. The squares shown in (**b**–**d**) represent the autocorrelation traces. Solid lines represent the Gaussian fits of experimentally obtained spectra.

photodetectors, and lasers. Meanwhile, in our earlier work, we have already demonstrated the application of such species for HHG of the chirp-free 35 fs pulses using the same samples, which were ablated by nanosecond and picosecond heating pulses [73]. In this subsection, we analyze the harmonics emission from LIPs of reported NCs using chirped TCP and SCP driving laser pulses and compare the results with chirp-free pulses.

The spectral profiles of chirp-free and chirped pulses were measured using a USB spectrometer (Ocean Optics) and are shown in Fig. 8a. All these pulses possess the same spectral components. Meanwhile, their distribution along the laser pulses significantly differs from each other. The blue and red components were equally distributed along the temporal shape of chirp-free 35 fs pulses (Fig. 8b). The spectral distribution along the negatively and positively chirped 135 fs pulses is shown in Fig. 8c, d, respectively. The blue and red components are moved toward the leading front and the tailing part of the pulses, respectively, for negatively chirped pulses. Whereas, for positively chirped 135 fs pulses, the reverse pattern is seen compared with the negatively chirped pulses. The red component is moved toward leading front of pulse, while blue component of spectrum is concentrated at the tailing part of the laser pulse.

Figure 9a, b show 2D color map and Figure 9c, d depict the corresponding line profiles of HHG spectra from 2D NCs generated by two-color pump and single-color pump of LIPs using chirp-free 35 fs pulses, negatively and positively chirped 135 fs pulses, respectively. The intensities of chirped pulses during propagation through the LIPs were 0.9×10^{14} W/cm^2. The laser intensity of the chirp-free 35-fs pulse was 4.0×10^{14} W/cm^2. Similar pulse energies (0.6 mJ) of the driving pulses were used in the case of chirp-free and chirped pulses. The harmonics shifted toward shorter and longer wavelengths in the case of

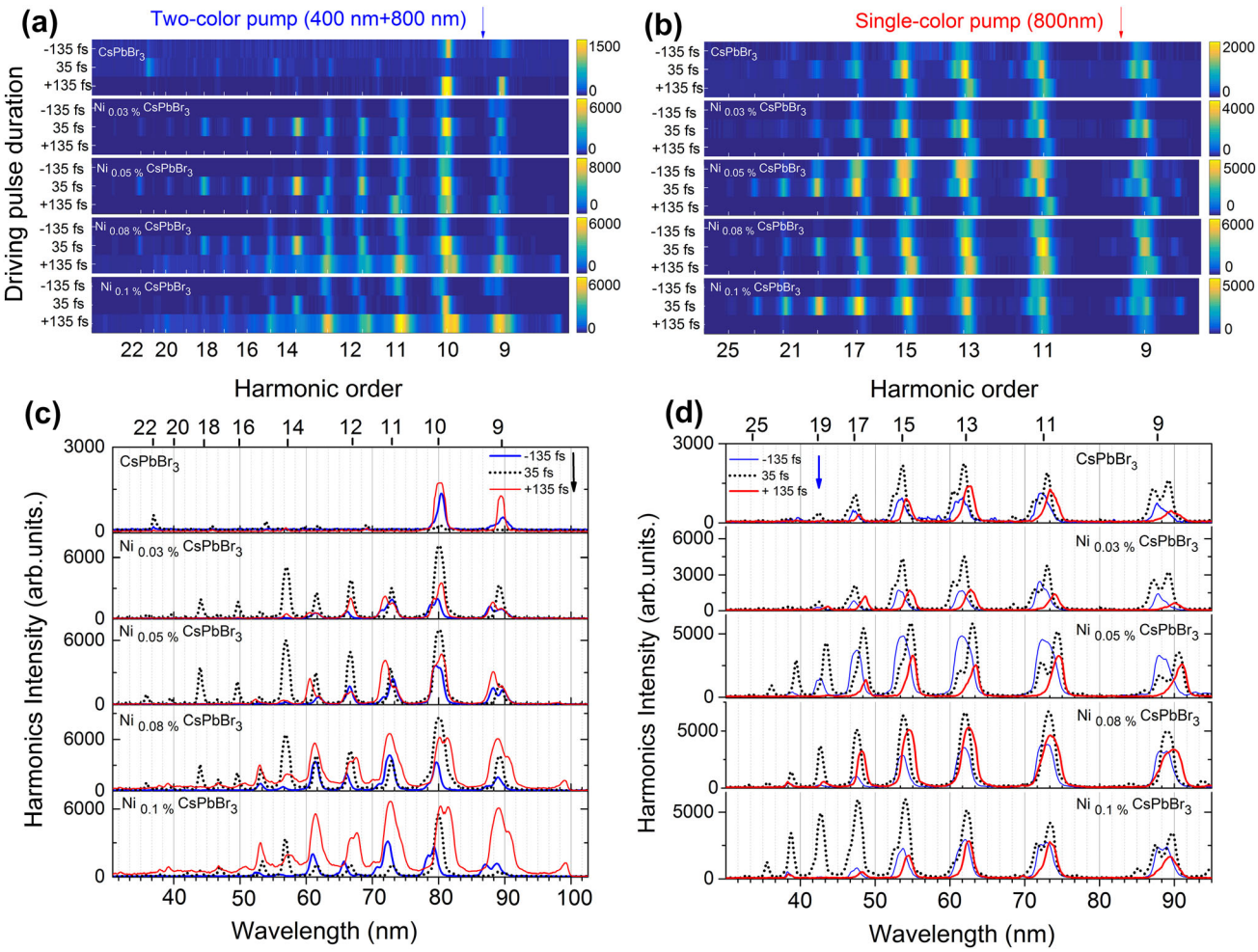

Figure 9 **a**, **b** 2D color map and **c**, **d** corresponding line profiles of Harmonic spectra from 2D nanocrystals generated by two-color pump and single-color pump of LIPs using chirp-free 35 fs pulses, negatively and positively chirped 135 fs pulses, respectively.

negatively and positively chirped driving laser pulses, respectively. For example, tenth harmonic (10H) in the case of TCP and ninth harmonic (9H) in the case of SCP of plasma showed ~0.30 and ~0.85 nm blue shifts, in the case of negatively chirped driving laser pulses with regard to the harmonics generated using chirp-free pulses. The leading parts of negatively and positively chirped DPs produced the harmonics from the blue and red spectral components, respectively, which led to the blueshift and redshift of harmonics. Therefore, one can finely control the shift of harmonics by changing the chirp of driving laser pulses. These modifications of harmonic spectra can find application in nonlinear spectroscopy of materials using tunable coherent XUV pulses.

The cut-off of harmonics is reduced for chirped pulses due to a decrease in the peak intensity of DPs. In the case of SCP, the chirp-free pulses produced maximum harmonic cut-off compared with chirped pulses. Also, for all samples, the even harmonics have higher intensities than odd harmonics. Higher intensity of the harmonics is attributed to the shorter wavelength sources (400 nm) compared with the 800 nm radiation, which is related to the growth of ponderomotive energy (U_p) of DP. In other words, the enhancement of harmonic yield is proportional to λ^{-5} or λ^{-6} [90–92]. Whereas, the cut-off of harmonics is proportional to $\sim\lambda^2$, since the energy cut-off is given by $E_{cut-off} = I_p + 3.17U_p$. Where I_p is the ionization potential, $U_p = 9.33\times10^{-14}\, I\,(W/cm^2)\,\lambda^2\,(\mu m)$, and I is the laser intensity [93].

Below we summarize our studies. The addition of Ni-dopants to the $CsPbBr_3$ NCs demonstrated significant changes in the NLO properties at different excitation wavelengths. In our earlier work [17] (800 nm, Z-scan measurements), the nonlinear absorption

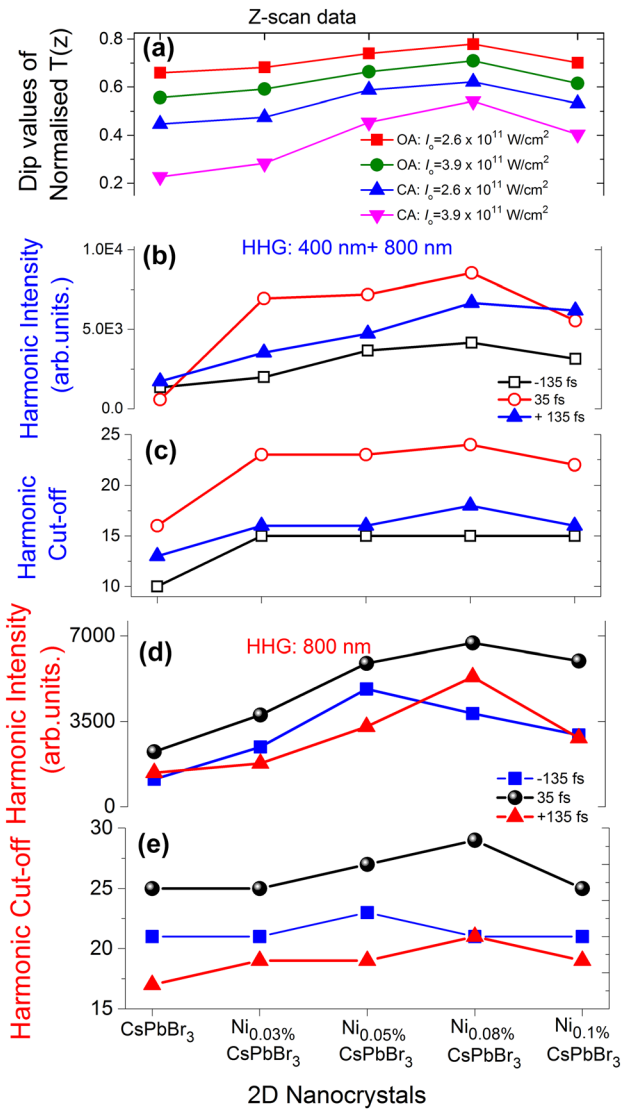

Figure 10 Summary graphs of the NLO response of studied samples versus the concentration of Ni. **a** Valley values of normalized T(z) for OA and CA measurements at 400 nm. **b–e** Harmonics intensity and cut-off for TCP and SCP chirp free and chirped driving pulses (see text).

coefficients and nonlinear refractive indices are increased with % change of Ni compared to the pure NCs. In contrast, in the current case with excitation by 400 nm pulses, the NLO coefficients are decreased. However, in this case the Ni dopants possess a self-defocusing effect, and in both cases, i.e., for 400 nm (only Ni contribution, current work) and 800 nm (earlier work [17]), we observed the incremental variation of γ. In both cases, the incremental trend is almost similar to HHG yields from the same studied samples for TCP (800 nm+400 nm) and SCP (800 nm).

In the case of HHG using TCP, the harmonic generation originates from both excitation wavelengths, i.e., from 800 nm and 400 nm pumps. Therefore, we have shown that higher nonlinear refractive indices for Ni-doped NCs correlate with higher HHG yields from the plasma plumes composed of the components of Ni+$CsPbBr_3$. Adding Ni to pure $CsPbBr_3$ could enhance the NLO response in terms of γ for 800 nm and 400 nm measured using Z-scan technique, and a similar behavior is also achieved for HHG yields for both driving schemes (SCP and TCP).

Meanwhile, by considering the nonlinear absorption, the Ni dopants demonstrate SA at higher intensities. In Fig. 6a, we showed the calculated I_{sat} and I_o/I_{sat} ratios for Ni NCs. The I_o/I_{sat} and γ dependencies look similar. Figure 10a shows the values of valleys in the OA and CA normalized transmittances; these curves are similar to the HHG curves for the samples shown in Figs. 10b–e. Finally, we can summarize that the NLO coefficients measured by Z-scan technique using 800 and 400 nm excitation wavelengths and HHG yields demonstrate similar tendency with variation of the Ni concentration.

Conclusions

In this work, we have explored the third-order NLO properties of pure $CsPbBr_3$ and Ni-doped $CsPbBr_3$ NCs using 400 nm, 60 fs, 1 kHz laser pulses. We also demonstrated the enhanced high-order harmonics generation in the plasmas produced on the surfaces of the latter species compared with the pristine NCs using different configurations of the driving pulses. The OA Z-scan measurements have shown that pure $CsPbBr_3$ NCs possess SA and RSA at lower and higher intensities of laser pulses, respectively. These samples have shown a self-focusing effect. However, the nonlinear absorption and refraction decreased for Ni-doped $CsPbBr_3$ NCs due to the opposite NLO properties of Ni dopants with regard to the $CsPbBr_3$ due to the growing influence of the SA and self-defocusing attributed to the Ni. In addition, we have examined the high-order harmonics emission from the LIPs of these NCs using TCP and SCP chirp-free and chirped driving laser pulses. The Ni-dopants have increased the harmonic cut-off and yield from the corresponding plasmas. We have also demonstrated the advantages of chirped laser pulses for

tuning the harmonics, which might be helpful for the XUV nonlinear spectroscopy of different materials. In summary, our detailed studies have demonstrated that β and γ values for combined $NiCsPbBr_3$ NCs are decreased compared to pure $CsPbBr_3$ NCs. However, if we consider NLO coefficients for Ni NCs, the γ values are increased with the growth of Ni doping concentration. The same tendency was observed in the harmonics yield and cut-off for both SCP and TCP of LIPs. Thus, the correlation between the low-order NLO properties and HHG of similar materials was demonstrated.

Acknowledgements

This work is supported by The Innovation Grant of Changchun Institute of Optics, Fine Mechanics and Physics (CIOMP), National Natural Science Foundation of China-(12004380, 62121005) Jilin Provincial Science and Technology Development Project (YDZJ202102CXJD002), Development Program of the Science and Technology of Jilin Province (20200802001GH). Srinivasa Rao Konda acknowledges the Chinese Academy of Sciences President's International Fellowship Initiative (2021PM0036). R. A. Ganeev acknowledges the European Regional Development Fund (1.1.1.5/19/A/003) and the Chinese Academy of Sciences President's International Fellowship Initiative (2022VMA0012). Venugopal Rao Soma acknowledges the financial support from DRDO, India.

Authors contributions

SRK contributed to conceptualization, methodology, writing—original draft, writing—review and editing. VRS contributed to conceptualization, writing—review and editing. RAG contributed to conceptualization, writing—review and editing. MB and RK contributed to synthesis of samples, characterization of nanocrystals. WL contributed to conceptualization, supervision, funding acquisition.

Data availability

The data that support the findings presented here are available from the authors upon reasonable request.

Declarations

Conflict of interest The authors declare no conflicts of interest.

References

[1] Yu S, Liu P, Xiao S (2021) A review of main characterization methods for identifying two-dimensional organic–inorganic halide perovskites. J Mater Sci 56:11656–11681. https://doi.org/10.1007/s10853-021-06038-2

[2] Wang G, Mei S, Liao J et al (2021) Advances of nonlinear photonics in low-dimensional halide perovskites. Small 2100809:1–21. https://doi.org/10.1002/smll.202100809

[3] Huang YT, Kavanagh SR, Scanlon DO et al (2021) Perovskite-inspired materials for photovoltaics and beyond-from design to devices. Nanotechnology 32:132004. https://doi.org/10.1088/1361-6528/abcf6d

[4] Chen W, Zhang F, Wang C et al (2021) Nonlinear photonics using low-dimensional metal-halide perovskites: recent advances and future challenges. Adv Mater 33:1–46. https://doi.org/10.1002/adma.202004446

[5] Shen W, Chen J, Wu J et al (2021) Nonlinear optics in lead halide perovskites: mechanisms and applications. ACS Photonics 8:113–124. https://doi.org/10.1021/acsphotonics.0c01501

[6] Li M, Wang C, Wang L, Zhang H (2021) Colloidal semiconductor nanocrystals: synthesis, optical nonlinearity, and related device applications. J Mater Chem C 9:6686–6721. https://doi.org/10.1039/d0tc05771a

[7] Chen M, Wang J, Yin F et al (2021) Strategically integrating quantum dots into organic and perovskite solar cells. J Mater Chem A 9:4505–4527. https://doi.org/10.1039/d0ta11336k

[8] Chen C, Zheng S, Song H (2021) Photon management to reduce energy loss in perovskite solar cells. Chem Soc Rev 50:7250–7329. https://doi.org/10.1039/d0cs01488e

[9] Tailor NK, Kar S, Mishra P et al (2021) Advances in lead-free perovskite single crystals: fundamentals and applications. ACS Mater Lett 3:1025–1080. https://doi.org/10.1021/acsmaterialslett.1c00242

[10] Feng W, Liao JF, Chang X et al (2021) Perovskite crystals redissolution strategy for affordable, reproducible, efficient and stable perovskite photovoltaics. Mater Today 50:199–223. https://doi.org/10.1016/j.mattod.2.doi:10.1016/j.mattod.2021.05.020

[11] Hu Z, Liu Z, Zhan Z et al (2021) Advances in metal halide perovskite lasers: synthetic strategies, morphology control, and lasing emission. Adv Photonics 3:1–23. https://doi.org/10.1117/1.ap.3.3.034002

[12] Dey A, Ye J, De A et al (2021) State of the art and prospects for halide perovskite nanocrystals. ACS Nano 15:10775–10981. https://doi.org/10.1021/acsnano.0c08903

[13] Cao Z, Hu F, Zhang C et al (2020) Optical studies of semiconductor perovskite nanocrystals for classical optoelectronic applications and quantum information technologies: a review. Adv Photonics 2:8–10. https://doi.org/10.1117/1.ap.2.5.054001

[14] Chen Z, Segev M (2021) Highlighting photonics: looking into the next decade. eLight 1:1–12. https://doi.org/10.1186/s43593-021-00002-y

[15] Ferrando A, Martínez Pastor JP, Suárez I (2018) Toward metal halide perovskite nonlinear photonics. J Phys Chem Lett 9:5612–5623. https://doi.org/10.1021/acs.jpclett.8b01967

[16] Xu J, Li X, Xiong J et al (2019) Halide Perovskites for nonlinear Optics. Adv Mater 32:1–13. https://doi.org/10.1002/adma.201806736

[17] Ketavath R, Katturi NK, Ghugal SG et al (2019) Deciphering the ultrafast nonlinear optical properties and dynamics of pristine and Ni-doped $CsPbBr_3$ colloidal two-dimensional nanocrystals. J Phys Chem Lett 10:5577–5584. https://doi.org/10.1021/acs.jpclett.9b02244

[18] Chen W, Bhaumik S, Veldhuis SA et al (2017) Giant five-photon absorption from multidimensional core-shell halide perovskite colloidal nanocrystals. Nat Commun 8:15198. https://doi.org/10.1038/ncomms15198

[19] Li L, Shang X, Wang S et al (2018) bilayered hybrid perovskite ferroelectric with giant two-photon absorption. J Am Chem Soc 140:6806–6809. https://doi.org/10.1021/jacs.8b04014

[20] Saouma FO, Park DY, Kim SH et al (2017) Multiphoton absorption coefficients of organic-inorganic lead halide perovskites $CH_3NH_3PbX_3$ (X = Cl, Br, I) single crystals. Chem Mater 29:6876–6882. https://doi.org/10.1021/acs.chemmater.7b02110

[21] Han Q, Wu W, Liu W et al (2018) Two-photon absorption and upconversion luminescence of colloidal $CsPbX_3$ quantum dots. Opt Mater (Amst) 75:880–886. https://doi.org/10.1016/j.optmat.2017.12.006

[22] He T, Li J, Ren C et al (2017) Strong two-photon absorption of Mn-doped $CsPbCl_3$ perovskite nanocrystals. Appl Phys Lett 111:1–5. https://doi.org/10.1063/1.5008437

[23] Xu Y, Chen Q, Zhang C et al (2016) Two-photon-pumped perovskite semiconductor nanocrystal lasers. J Am Chem Soc 138:3761–3768. https://doi.org/10.1021/jacs.5b12662

[24] Walters G, Sutherland BR, Hoogland S et al (2015) Two-photon absorption in organometallic bromide perovskites. ACS Nano 9:9340–9346. https://doi.org/10.1021/acsnano.5b03308

[25] Wang Y, Li X, Zhao X et al (2016) Nonlinear absorption and low-threshold multiphoton pumped stimulated emission from all-inorganic perovskite nanocrystals. Nano Lett 16:448–453. https://doi.org/10.1021/acs.nanolett.5b04110

[26] Chen W, Zhang S, Zhou M et al (2019) Two-photon absorption-based upconverted circularly polarized luminescence generated in chiral perovskite nanocrystals. J Phys Chem Lett 10:3290–3295. https://doi.org/10.1021/acs.jpclett.9b01224

[27] Zou S, Yang G, Yang T et al (2018) Template-free synthesis of high-yield Fe-doped cesium lead halide perovskite ultralong microwires with enhanced two-photon absorption. J Phys Chem Lett 9:4878–4885. https://doi.org/10.1021/acs.jpclett.8b02127

[28] Nagamine G, Rocha JO, Bonato LG et al (2018) Two-photon absorption and two-photon-induced gain in perovskite quantum dots. J Phys Chem Lett 9:3478–3484. https://doi.org/10.1021/acs.jpclett.8b01127

[29] Saouma FO, Stoumpos CC, Kanatzidis MG et al (2017) Multiphoton absorption order of $CsPbBr_3$ as determined by wavelength-dependent nonlinear optical spectroscopy. J Phys Chem Lett 8:4912–4917. https://doi.org/10.1021/acs.jpclett.7b02286

[30] Pramanik A, Gates K, Gao Y et al (2019) Several orders-of-magnitude enhancement of multiphoton absorption property for $CsPbX_3$ perovskite quantum dots by manipulating halide stoichiometry. J Phys Chem C 123:5150–5156. https://doi.org/10.1021/acs.jpcc.9b01108

[31] Suárez I, Vallés-Pelarda M, Gualdrón-Reyes AF et al (2019) Outstanding nonlinear optical properties of methylammonium- and Cs-PbX_3 (X = Br, I, and Br-I) perovskites: polycrystalline thin films and nanoparticles. APL Mater. https://doi.org/10.1063/1.5090926

[32] Lu WG, Chen C, Han D et al (2016) Nonlinear optical properties of colloidal $CH_3NH_3PbBr_3$ and $CsPbBr_3$ quantum dots: a comparison study using Z-Scan technique. Adv Opt Mater 4:1732–1737. https://doi.org/10.1002/adom.201600322

[33] Li J, Dong H, Xu B et al (2017) $CsPbBr_3$ perovskite quantum dots: saturable absorption properties and passively Q-switched visible lasers. Photonics Res 5:457. https://doi.org/10.1364/prj.5.000457

[34] Rutledge J, Catanese A, Hickstein DD et al (2021) Broadband ultraviolet-visible frequency combs from cascaded high-harmonic generation in quasi-phase-matched waveguides. J Opt Soc Am B 38:2252. https://doi.org/10.1364/josab.427086

[35] Khairulin IR, Emelin MY, Ryabikin MY (2021) Ultrahigh-order harmonic generation in the subnanometer wavelength

range: the role of finite atomic size. J Opt Soc Am B 38:2329. https://doi.org/10.1364/josab.427812

[36] Major B, Ghafur O, Kovács K et al (2021) Compact intense extreme-ultraviolet source. Optica 8:960. https://doi.org/10.1364/optica.421564

[37] Bengs U, Zhavoronkov N (2021) Elliptically polarized high-harmonic radiation for production of isolated attosecond pulses. Sci Rep 11:1–10. https://doi.org/10.1038/s41598-021-88557-1

[38] Sanari Y, Hirori H, Aharen T et al (2020) Role of virtual band population for high harmonic generation in solids. Phys Rev B 102:41125. https://doi.org/10.1103/PhysRevB.102.041125

[39] Chang Z, Corkum P (2010) Attosecond photon sources: the first decade and beyond [Invited]. JOptSocAm B 27:9–17. https://doi.org/10.1364/JOSAB.27.0000B9

[40] Feng X, Gilbertson S, Mashiko H et al (2009) Generation of isolated attosecond pulses with 20 to 28 femtosecond lasers. Phys Rev Lett 103:183901. https://doi.org/10.1103/PhysRevLett.103.183901

[41] Li Z, Brown G, Ko DH et al (2017) Perturbative high harmonic wave front control. Phys Rev Lett 118:33905. https://doi.org/10.1103/PhysRevLett.118.033905

[42] Kong F, Zhang C, Bouchard F et al (2017) Controlling the orbital angular momentum of high harmonic vortices. Nat Commun 8:14970. https://doi.org/10.1038/ncomms14970

[43] Fareed MA, Strelkov VV, Thire N et al (2017) High-order harmonic generation from the dressed autoionizing states. Nat Commun 8:16061. https://doi.org/10.1038/ncomms16061

[44] Elouga Bom LB, Haessler S, Gobert O et al (2011) Attosecond emission from chromium plasma. Opt Expr 19:3677–3685. https://doi.org/10.1364/OE.19.003677

[45] Pertot Y, Chen S, Khan SD et al (2012) Generation of continuum high-order harmonics from carbon plasma using double optical gating. J Phys B At Mol Opt Phys 45:074017. https://doi.org/10.1088/0953-4075/45/7/074017

[46] Rosenthal N, Marcus G (2015) Discriminating between the role of phase matching and that of the single-atom response in resonance plasma-plume high-order harmonic generation. Phys Rev Lett 133901:1–4. https://doi.org/10.1103/PhysRevLett.115.133901

[47] Liang J, Lai YH, Fu W et al (2021) Distinguishing monomer and nanoparticle contributions to high-harmonic emission from laser-ablated plumes. Opt Express 29:23421. https://doi.org/10.1364/oe.428652

[48] Ganeev RA (2009) Generation of high-order harmonics of high-power lasers in plasmas produced under irradiation of solid target surfaces by a prepulse. Physics-Uspekhi 52:55–77. https://doi.org/10.3367/UFNe.0179.200901c.0065

[49] Suzuki M, Baba M, Kuroda H et al (2007) Intense exact resonance enhancement of single-high-harmonic from an antimony ion by using Ti: Sapphire laser at 37 nm. Opt Expr 15:1161–1166. https://doi.org/10.1364/OE.15.001161

[50] Ganeev RA, Suzuki M, Baba M, Kuroda H (2005) Generation of strong coherent extreme ultraviolet radiation from the laser plasma produced on the surface of solid targets. Appl Phys B 81:1081–1089. https://doi.org/10.1007/s00340-005-1993-0

[51] Ozaki T, Elouga Bom LB, Ganeev RA et al (2007) Intense harmonic generation from silver ablation. Laser Part Beams 25:321–325. https://doi.org/10.1017/S0263034607000201

[52] Ganeev RA, Bom LBE, Wong MCH et al (2009) High-order harmonic generation from C60-rich plasma. Phys Rev A 80:043808

[53] Hutchison C, Ganeev RA, Witting T et al (2012) Stable generation of high-order harmonics of femtosecond laser radiation from laser produced plasma plumes at 1 kHz pulse repetition rate. Opt Lett 37:2064–2066. https://doi.org/10.1364/OL.37.002064

[54] Ganeev RA, Suzuki M, Baba M, Kuroda H (2005) High-order harmonic generation from carbon plasma. J Opt Soc Am B 22:1927–1933. https://doi.org/10.1364/JOSAB.22.001927

[55] Singhal H, Ganeev RA, Naik PA et al (2010) Study of high-order harmonic generation from nanoparticles. J Phys B At Mol Opt Phys 43:025603. https://doi.org/10.1088/0953-4075/43/2/025603

[56] Ganeev RA, Hutchison C, Witting T et al (2012) High-order harmonic generation in graphite plasma plumes using ultrashort laser pulses: a systematic analysis of harmonic radiation and plasma conditions. J Phys B At Mol Opt Phys 45:165402. https://doi.org/10.1088/0953-4075/45/16/165402

[57] Fu Y, Ganeev RA, Boltaev GS et al (2019) Low- and high-order nonlinear optical properties of Ag_2S quantum dot thin films. Nanophotonics 8:849–858. https://doi.org/10.1515/nanoph-2018-0213

[58] Légaré K, Safaei R, Barrette G et al (2021) Raman red-shift compressor: a simple approach for scaling the high harmonic generation cut-off. Adv Photonics Res. 2:2100113. https://doi.org/10.1002/adpr.202100113

[59] Lee DG, Kim JH, Hong KH, Nam CH (2001) Coherent control of high-order harmonics with chirped femtosecond laser pulses. Phys Rev Lett 87:2439021–2439024. https://doi.org/10.1103/PhysRevLett.87.243902

[60] Tosa V, Kim HT, Kim IJ, Nam CH (2005) High-order harmonic generation by chirped and self-guided femtosecond

laser pulses. I. Spatial and spectral analysis. Phys Rev A 71:1–7. https://doi.org/10.1103/PhysRevA.71.063807

[61] Han J-X, Wang J, Qiao Y et al (2019) Significantly enhanced conversion efficiency of high-order harmonic generation by introducing chirped laser pulses into scheme of spatially inhomogeneous field. Opt Express 27:8768. https://doi.org/10.1364/oe.27.008768

[62] Fan JG, Miao XY, Jia XF (2021) Control of the high-order harmonic generation by sculpting waveforms with chirp in solids. Chem Phys Lett 762:138136. https://doi.org/10.1016/j.cplett.2020.138136

[63] Neyra E, Videla F, Pérez-Hernández JA et al (2016) High-order harmonic generation driven by chirped laser pulses induced by linear and non linear phenomena. Eur Phys J D 70:2–8. https://doi.org/10.1140/epjd/e2016-70320-5

[64] Yun CX, Teng H, Zhang W et al (2010) High-order harmonics generation by few-cycle and multi-cycle femtosecond laser pulses. Chinese Phys B 19:1–4. https://doi.org/10.1088/1674-1056/19/12/124210

[65] Hussain M, Kaassamani S, Auguste T et al (2021) Spectral control of high order harmonics through non-linear propagation effects. Appl Phys Lett 119:071101. https://doi.org/10.1063/5.0053152

[66] Ganeev RA, Singhal H, Naik PA et al (2007) Optimization of the high-order harmonics generated from silver plasma. Appl Phys B Lasers Opt 87:243–247. https://doi.org/10.1007/s00340-007-2583-0

[67] Mikaelsson S, Vogelsang J, Guo C et al (2020) A high-repetition rate attosecond light source for time-resolved coincidence spectroscopy. Nanophotonics 10:117–128. https://doi.org/10.1515/nanoph-2020-0424

[68] Hadrich S, Krebs M, Hoffmann A et al (2015) Exploring new avenues in high repetition rate table-top coherent extreme ultraviolet sources. Light Sci Appl 4:e320. https://doi.org/10.1038/lsa.2015.93

[69] Li JJ, Lu J, Chew A et al (2020) Attosecond science based on high harmonic generation from gases and solids. Nat Commun 11:2748. https://doi.org/10.1038/s41467-020-16480-6

[70] Kanda N, Imahoko T, Yoshida K et al (2020) Opening a new route to multiport coherent XUV sources via intracavity high-order harmonic generation. Light Sci Appl 9:168. https://doi.org/10.1038/s41377-020-00405-5

[71] Kim H, Bae SR, Lee TH et al (2021) Enhanced optical properties and stability of $CsPbBr_3$ nanocrystals through nickel doping. Adv Funct Mater 31:1–9. https://doi.org/10.1002/adfm.202102770

[72] van der Stam W, Geuchies JJ, Altantzis T et al (2017) Highly emissive divalent-ion-doped colloidal $CsPb_{1-x}M_xBr_3$ perovskite nanocrystals through cation exchange. J Am Chem Soc 139:4087–4097. https://doi.org/10.1021/jacs.6b13079

[73] Konda SR, Soma VR, Banavoth M et al (2021) High harmonic generation from laser-induced plasmas of Ni-doped $CsPbBr_3$ nanocrystals: implications for extreme ultraviolet light sources. ACS Appl Nano Mater 4:8292–8301. https://doi.org/10.1021/acsanm.1c01490

[74] Chapple PB, Staromlynska J, Hermann JA et al (1997) Single-beam Z-scan: measurement techniques and analysis. J Nonlinear Opt Phys Mater 06:251–293. https://doi.org/10.1142/S0218863597000204

[75] Liu X, Guo S, Wang H, Hou L (2001) Theoretical study on the closed-aperture Z-scan curves in the materials with nonlinear refraction and strong nonlinear absorption. Opt Commun 197:431–437. https://doi.org/10.1016/S0030-4018(01)01406-7

[76] Krishna BG, Ghosh DS, Tiwari S (2021) Tuning optical properties of $CsPbBr_3$ perovskite nanocrystals through silver doping. J Mater Sci Mater Electron In Press: https://doi.org/10.1007/s10854-021-07447-4

[77] Zhang J, Jiang T, Zheng X et al (2017) Thickness-dependent nonlinear optical properties of $CsPbBr_3$ perovskite nanosheets. Opt Lett 42:3371. https://doi.org/10.1364/ol.42.003371

[78] Zhou Y, Hu Z, Li Y et al (2016) $CsPbBr_3$ nanocrystal saturable absorber for mode-locking ytterbium fiber laser. Appl Phys Lett 108:3–7. https://doi.org/10.1063/1.4955037

[79] Clark DJ, Stoumpos CC, Saouma FO et al (2016) Polarization-selective three-photon absorption and subsequent photoluminescence in $CsPbBr_3$ single crystal at room temperature. Phys Rev B 93:1–8. https://doi.org/10.1103/PhysRevB.93.195202

[80] Mushtaq A, Pradhan B, Kushavah D et al (2021) Third-order nonlinear optical properties and saturation of two-photon absorption in lead-free double perovskite nanocrystals under femtosecond excitation. ACS Photonics 8:3365–3374. https://doi.org/10.1021/acsphotonics.1c01351

[81] Huang L, Yu B, Zhu F et al (2022) Spin-coating thermal-pressed strategy for the preparation of inorganic perovskite quasi-single-crystal thin films with giant single-/two-photon responses. Nano Energy 92:106719. https://doi.org/10.1016/j.nanoen.2021.106719

[82] Priyadarshini M, Acharyya JN, Mahajan S, Vijaya Prakash G (2021) Optical nonlinearities in chemically synthesized and femtosecond laser fabricated gold nanoparticle colloidal solutions. Opt Laser Technol 139:107008. https://doi.org/10.1016/j.optlastec.2021.107008

[83] Mondal K, Biswas S, Singha T et al (2021) Unusual higher-order nonlinear optical properties in Au-coated triangular

Ag-Au nanostructures. Opt Lett 46:4879. https://doi.org/10.1364/ol.439398

[84] Zhu C, Wang L, Zhao D et al (2021) Multiphoton upconversion and non-resonant optical nonlinearity in perovskite quantum dot doped glasses. Opt Lett 46:5216. https://doi.org/10.1364/ol.438340

[85] Fu Y, Ganeev RA, Krishnendu PS et al (2019) Size-dependent off-resonant nonlinear optical properties of gold nanoparticles and demonstration of efficient optical limiting. Opt Mater Express 9:976–991. https://doi.org/10.1364/OME.9.000976

[86] Zhang K, Ganeev RA, Rao KS et al (2019) (2019) Interaction of pulses of different duration with chemically prepared silver nanoparticles: analysis of optical nonlinearities. J Nanomater 6056528:12. https://doi.org/10.1155/2019/6056528

[87] Akkerman QA, Gandini M, Di Stasio F et al (2016) Strongly emissive perovskite nanocrystal inks for high-voltage solar cells. Nat Energy 2:1–7. https://doi.org/10.1063/1.334537

[88] Hirasawa M, Ishihara T, Goto T et al (1994) Magnetoabsorption of the lowest exciton in perovskite-type compound $(CH_3NH_3)PbI_3$. Phys B Phys Condens Matter 201:427–430. https://doi.org/10.1016/0921-4526(94)91130-4

[89] Pavliuk MV, Fernandes DLA, El-Zohry AM et al (2016) Magnetic manipulation of spontaneous emission from inorganic $CsPbBr_3$ perovskites nanocrystals. Adv Opt Mater 4:2004–2008. https://doi.org/10.1002/adom.201600611

[90] Frolov MV, Manakov NL, Starace AF (2008) Wavelength scaling of high-harmonic yield: threshold phenomena and bound state symmetry dependence. Phys Rev Lett 100:1–4. https://doi.org/10.1103/PhysRevLett.100.173001

[91] Tate J, Auguste T, Muller HG et al (2007) Scaling of wavepacket dynamics in an intense midinfrared field. Phys Rev Lett 98:1–4. https://doi.org/10.1103/PhysRevLett.98.013901

[92] Frolov MV, Manakov NL, Xiong WH et al (2015) Scaling laws for high-order-harmonic generation with midinfrared laser pulses. Phys Rev A - At Mol Opt Phys 92:1–8. https://doi.org/10.1103/PhysRevA.92.023409

[93] Corkum PB (1993) Plasma perspective on strong field multiphoton ionization. Phys Rev Lett 71:1994–1997. https://doi.org/10.1103/PhysRevLett.71.1994